Chapter 17
Growth and Properties of Epitaxial Chromium Dioxide (CrO_2) Thin Films and Heterostructures

Guo-Xing Miao and Arunava Gupta

Abstract CrO_2 is a remarkable ferromagnetic material that is simultaneously an excellent metal for majority spin electrons and an insulator for minority spin electrons [1–3]. For this reason, CrO_2 is called a half-metal, and in fact, it is the only one experimentally demonstrated [4–6]. Because of this, CrO_2 has received considerable interest for spintronic applications in recent years. Band structure calculations have shown that the conduction bands in the spin minority channel of this system are completely shifted away from the Fermi level, resulting in 100% spin polarization. This makes it an attractive choice as a ferromagnetic material for spin-dependent devices such as spin injectors and spin detectors. In this chapter, we briefly describe the bonding characteristics in CrO_2, based on first principles band structure calculations, as well as discuss some of its intrinsic structural, electrical, and magnetic properties. The strain-induced magnetic anisotropy resulting from lattice mismatch with the substrates is also discussed. Finally, we provide some details regarding the fabrication of epitaxial rutile-based heterostructures and their transport properties in micron-sized tunnel junction and GMR devices.

17.1 Density of States (DOS) of Half-Metallic CrO_2 and the Double Exchange Mechanism

We use the DOS of half-metallic oxide (CrO_2), a non-magnetic metallic oxide (RuO_2), and an insulating oxide (TiO_2), all belonging to the rutile family, to illustrate the differences between a half-metal and other materials. Figure 17.1 illustrates the unit cell of a rutile structure. We choose TiO_2 (with the rutile structural polymorph) for comparison because Ti($Z = 22$) is very close to Cr(Z = 24) in the periodic table, and it is also the most common member within the rutile family.

A. Gupta (✉)
Center for Materials for Information Technology (MINT), The University of Alabama, Tuscaloosa, AL 35487, USA
e-mail: agupta@mint.ua.edu

J.P. Liu et al. (eds.), *Nanoscale Magnetic Materials and Applications*,
DOI 10.1007/978-0-387-85600-1_17, © Springer Science+Business Media, LLC 2009

Further, very high-quality single crystal substrates of TiO_2 with cuts of different orientations ((100), (110), and (001)) are available commercially. We choose RuO_2 as an example of a non-magnetic metallic rutile oxide. We can epitaxially grow thin films of these rutile oxides using the technique of chemical vapor deposition (CVD) and also form heteroepitaxial structures with each other.

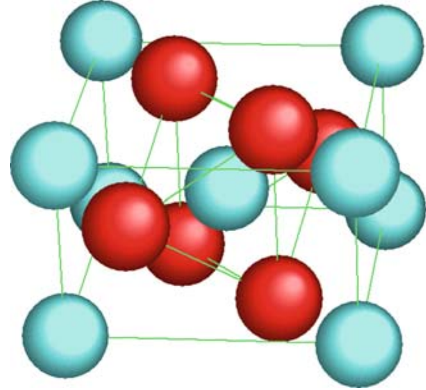

Fig. 17.1 The rutile crystal structure. The *dark spheres* indicate the O ions, and the *light spheres* indicate the cations (Ti, Cr, Sn, Ru, etc.) in the unit cell. The octahedral coordination of the central cation is depicted in the drawing

In the following examples of DOS results for various rutile oxides, we have carried out the calculations using the generalized gradient approximation (GGA) method in the VASP code allowing the atoms to relax to their equilibrium positions by minimizing the stress tensors acting on them. Figure 17.2 illustrates the total DOS for CrO_2, TiO_2, and RuO_2. The half-metallic nature of CrO_2 is apparent from comparing the three plots. The spin-up DOS of CrO_2 closely resembles the DOS of RuO_2, while the spin-down DOS of CrO_2 is similar to the DOS of TiO_2. Therefore, CrO_2 is metallic in its spin-up channel, and insulating in its spin-down channel, hence the name "half-metal." The *s*, *p*, and *d* electron sub-DOS of CrO_2 are also illustrated in Fig. 17.2. Below the Fermi energy in the energy range $-8\text{eV} < E < -2\text{eV}$, the *p* and *d* electron DOS have similar shapes, although with differing intensities. As a consequence, there is covalent bonding between the Cr($3d$) and the O($2p$) electrons. The crystalline field due to the octahedral coordination of the Cr ions splits the Cr$3d$ orbitals into t_{2g} and e_g sub-bands, occupying the energy range $-2\text{eV} < E < -2\text{eV}$ and $2\text{eV} < E < -2\text{eV}$, respectively. The spin-down DOS is rigidly shifted because of exchange interaction by approximately $2rmeV$, resulting in a band gap of about 2eV in the spin minority channel. The local distortion of the CrO_6 octahedra further splits the t_{2g} bands into xy, $yz + zx$, and $yz-zx$ orbitals. Cr^{4+} (d^2) has two valence electrons. One of them, with xy character, is buried below the Fermi level (the DOS peak between $-$eV and 0eV) and strongly localized at each site. The other, with mainly $yz + zx$ character, lies across the Fermi level and is strongly hybridized with O$2p$ electrons. It has been proposed that such an electronic configuration makes CrO_2 "a self-doped double exchange ferromagnet" [3]. The valence electrons themselves provide the localized and mobile

electrons, and according to Hund's rule the free-moving electrons travel between sites and have the effect of ferromagnetically aligning the neighboring spins.

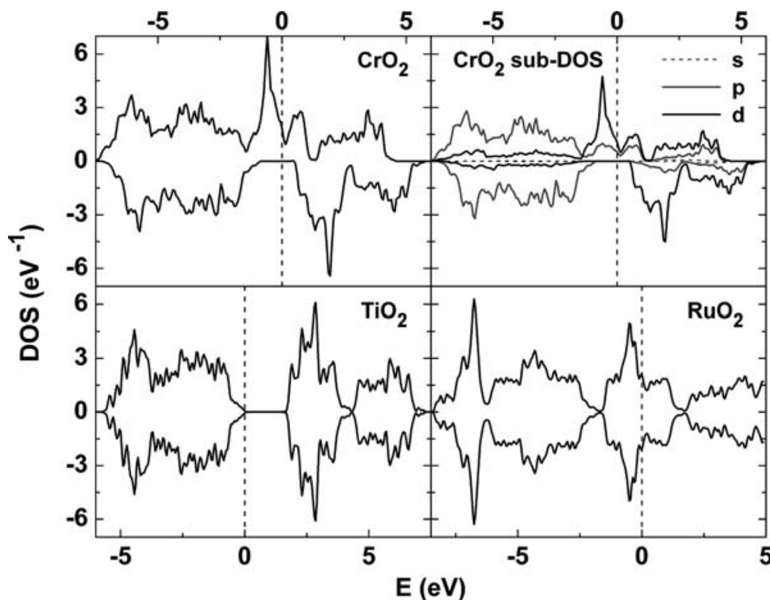

Fig. 17.2 The DOS for half-metallic CrO_2, metallic RuO_2, and insulating TiO_2. The angular momentum dependent sub-DOS of CrO_2 is also shown in the *upper right panel*. The Fermi level is defined as energy zero

17.2 Intrinsic Properties of Epitaxial CrO_2 Films

As mentioned earlier, CrO_2 has a tetragonal rutile structure with bulk lattice parameters of $a = b = 0.4421$ nm and $c = 0.2916$ nm The short c axis is a consequence of the distortion of the oxygen octahedral. Being a metastable phase, the nucleation of CrO_2 is critically dependent on the substrate lattice structure and the formation temperature. For aiding the nucleation and epitaxial growth of CrO_2, we choose an isostructural and well-lattice-matched substrate, namely (100)-TiO_2 with lattice parameters of $a = b = 0.4594$ nm, and $c = 0.2958$ nm We have deposited high-quality epitaxial CrO_2 thin films using a simple CVD reactor consisting of a quartz tube placed inside a two-zone furnace with independent temperature control of the two zones [7, 8]. Before film growth, the single crystal (100)-TiO_2 substrates are cleaned with organic solvents and dilute hydrofluoric (HF) acid solution and loaded into the CVD chamber. The films are grown at a substrate temperature of 400°C in the primary reaction zone, with the solid CrO_3 precursor being placed in the secondary zone of the furnace that is heated to about 260°C for sublimation. Oxygen is used as a carrier gas with a flow rate of 100 sccm.

Due to the difficulty in the formation of CrO_2 under ambient conditions, deposition during the CVD growth process occurs selectively on the lattice-matched TiO_2 substrate in a very narrow temperature window of $\pm 20\,^{\circ}$C, with the quartz tube and the susceptor remaining clean after the deposition. The selective deposition of CrO_2 [9, 10] can be exploited for the patterned growth of the material using TiO_2 substrates that are pre-patterned using SiO_2 [10]. The lattice match between the film and the substrate results in epitaxial strain in the film that can lead to significant modifications in the film properties. We will detail the influence of strain on the magnetic properties in the next section. Because the lattice parameters of rutile TiO_2 are larger than those for CrO_2 by 3.91 and 1.44% along the *b*- and the *c*-directions, respectively, the epitaxial films experience tensile stress in both in-plane directions and consequently shrink in the out-of-plane *a* direction. The strain increase shows up as a shift in the normal θ–2θ XRD peak to higher angles with decreasing film thickness (Fig. 17.3). In addition, we have performed off-axis XRD scans to determine the in-plane CrO_2 film lattice parameters for various thicknesses, and the strain relaxation roughly follows a $t^{1/3}$ dependence along all three lattice directions [11]. A slower relaxation rate than predicted by the equilibrium Matthews–Blakeslee (M-B) model [12] is commonly observed for epitaxial oxide films and has been attributed to kinetic barriers in the propagation and multiplication of the misfit dislocations needed for relaxation due to the ionic nature of the oxides [13, 14]. The strain relaxation mechanism in CrO_2 results in changes in the film quality with thickness. The inset to Fig. 17.3 illustrates the variation of the CrO_2 rocking curve FWHM of the (200) peak with film thickness. The peak width is a measure of the dispersion of the films out-of-plane alignment and is a direct indication of the film quality. A peak in the FWHM is observed for a film thickness of around 100 nm. For thinner films,

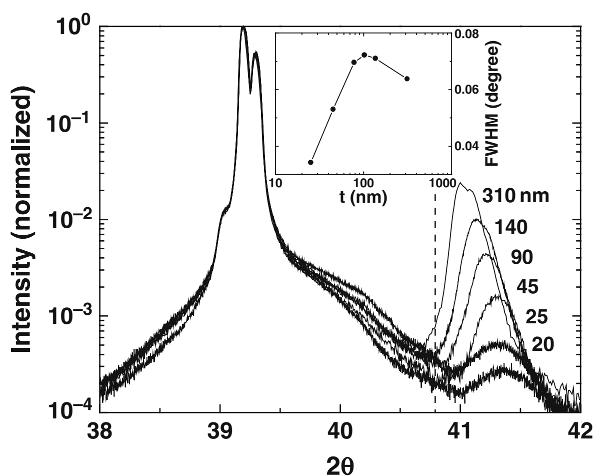

Fig. 17.3 XRD data around the (200) TiO_2 substrate and different thickness CrO_2 film peaks. *Dashed line* indicates the bulk CrO_2 (200) peak position. Inset shows the rocking curve FWHM

dislocations are not energetically favored, and the films grow coherently on the substrate. On the other hand, for thicker films, most of the strain is relaxed by dislocations, and the films grow relatively strain free. For films of intermediate thickness, the strain is only partially relaxed and is distributed relatively inhomogeneously across the thickness of the film. The effect of inhomogeneous strain distribution on the magnetic properties will be discussed in the next section.

The epitaxial CrO_2 films exhibit a strong anisotropy in the electrical conductivity between the long axes (*a*, *b*) and the short axis (*c*) directions, (Fig. 17.4). The resistivity for an 84 nm thick film along the *a*- and *c*-directions is 150 μΩ-cm and 200 μΩ-cm at room temperature, and 10.9 μΩ-cm and 5.6 μΩ-cm at 5 K, respectively. Apparently, transport along the *a*-direction is more favorable at RT, but it is overtaken by the *c*-direction at lower temperatures. The cross-over temperature between the two resistivity curves decreases with film thickness, and it ranges from 220 K for a 17 nm film to 130 K for a 400 nm film (Fig. 17.4 inset). The residual resistivity ratio (*rrr*) is much larger along the *c*- than in the *a*-direction. The larger *rrr* in the *c*-direction is not primarily a result of the increased phonon scattering, as normally interpreted for larger *rrr*. Instead it is a result of enhanced magnon scattering in this direction [15]. For comparison, similarly structured nonmagnetic RuO_2 films deposited by CVD on (100) TiO_2 substrates do not exhibit any significant transport anisotropy.

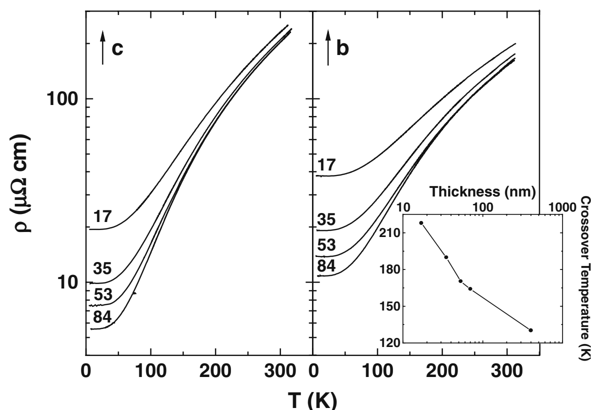

Fig. 17.4 Thickness dependence of the CrO_2 resistivity along the *c*- and *b*-axis directions. Thicknesses are marked in nanometers. Inset shows the cross-over temperature as a function of film thickness

The magnetic measurements presented here have been carried out on films of dimension $5\times5\,mm^2$, with the film thickness being no more than 2×10^{-4} of the lateral dimension. We thus expect the magnetization to be confined to the plane of the substrate with negligible in-plane demagnetizing field ($H_D < 0.5$Oe) and shape anisotropy. The thinnest film we have studied is about 9 nm thick (corresponding to about 40 atomic layers) and the surface anisotropy contribution, as is usually

observed in ultrathin (1–10 atomic layers) transition metal films, is not expected to be significant. For very thick films, the strain anisotropy can also be neglected. Figure 17.5 summarizes the magnetic properties of a bulk-like CrO_2 epitaxial film of 1 μm thickness. Irrespective of film thickness, the epitaxial (100) CrO_2 films that we have grown display a Curie temperature (T_C) of ∼390 K. The room temperature and 7 K saturation magnetization M_S have been determined to be 475 emu/cm^3 and 640 emu/cm^3, respectively. The corresponding anisotropy energy constant K_1 values are 2.2×10^5 and 4.5×10^5 erg/cm^3 (Fig. 17.5), and for K_2 are 4×10^4 and 3×10^4 erg/cm^3, respectively [16]. The anisotropy field values H_K are determined from the in-plane hard axis (*b*-axis) hysteresis loops, and the crystalline anisotropy energy constant K_1 is calculated from the relation $K_1 = H_K M_S/2$. Generally speaking, bulk CrO_2 is a relatively soft material as compared to most traditional ferromagnets. Its crystalline anisotropy energy along the *c*-axis decreases monotonically with temperature, rendering the bulk CrO_2 film's easy axis to be more closely aligned along the *c*-axis at lower temperatures due to the increased energy barrier in the hard *b*-axis direction. In competition, the strain arising from the misfit between the CrO_2thin film and the TiO_2 substrate creates an additional uniaxial

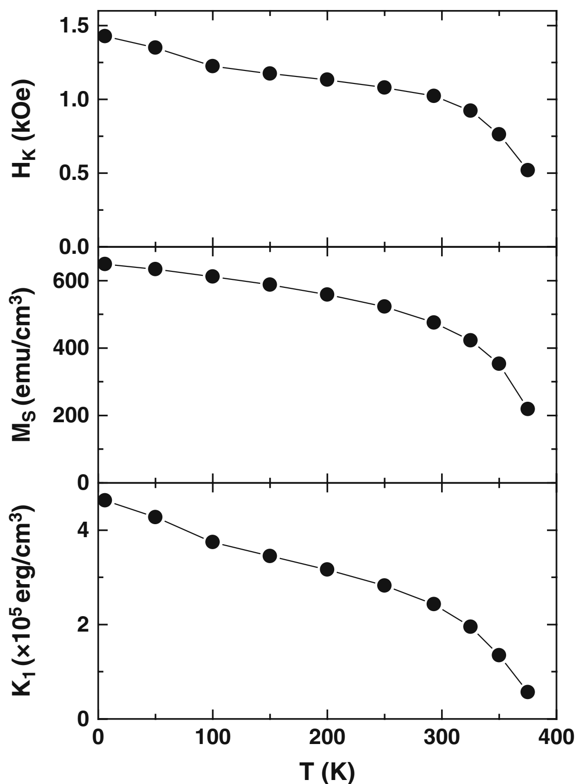

Fig. 17.5 Temperature dependence of the CrO_2 anisotropy field (H_K), saturation moment (M_S), and anisotropy energy constant (K_1), measured for a 1 μm thick CrO_2 film

anisotropy which favors the *b*-axis direction. With decreasing film thickness, this strain-induced anisotropy can become large enough to compete with and eventually surpass the intrinsic crystalline anisotropy. We will discuss the details of this effect in the next section.

17.3 Influence of Strain on the Magnetic Properties of CrO_2 Thin Films

For the practical implementation of CrO_2-based spintronic devices, it is important to gain a better understanding of its switching characteristics and magnetic anisotropy and to explore possible approaches to control these properties. With such knowledge, one can potentially realize independent switching of two separate CrO_2 layers, and thus manipulate the relative spin orientations of the layers. The latter is important for the operation of GMR and TMR-based devices. This section attempts to provide a comprehensive investigation of the magnetic properties of epitaxial CrO_2 thin films, with emphasis on the strong sensitivity of its magnetic anisotropy to strain and temperature.

17.3.1 Film Growth on Atomically Smooth TiO_2 Substrates

In this section, we discuss the magnetic properties of CrO_2 films deposited on atomically smooth (100)-TiO_2 substrates. A dilute HF treatment of the substrates is essential to achieve such smoothness. There are two competing anisotropies present in the as-deposited CrO_2 films – the magnetocrystalline and the strain anisotropy – that are considered significant. The former, a volume effect, is an intrinsic property of the material that favors the magnetic easy axis to orient along the in-plane *c*-direction. The latter is an interface effect, and highly strained thin films grown on (100)-TiO_2 substrates exhibit magnetic easy-axis alignment along the *b*-direction, since the lattice mismatch is larger along the *b* than in the *c*-axis direction (3.91% vs. 1.44%). We have found that the relative magnitude of these two anisotropies is dependent on the film thickness [17]. As illustrated in Fig. 17.6, the magnetic easy axis is aligned along the *c*-direction for thick CrO_2 films, but it becomes the hard axis for thin films due to the dominance of the strain anisotropy. The cross-over thickness is approximately 50 nm. Figure 17.7 clearly demonstrates the rotation of easy axis with film thickness, as evidenced from the 90° out of phase between the thick and thin films' magnetic switching properties. Based on simple estimates, one expects the ratio of the magnetocrystalline energy to the strain anisotropy energy to be approximately proportional to the film thickness t, which is related to the volume-to-surface ratio. We will show, based on a simplified model of residual strain in the film, that a more complex thickness dependence is appropriate in the heavily strained CrO_2 thin films.

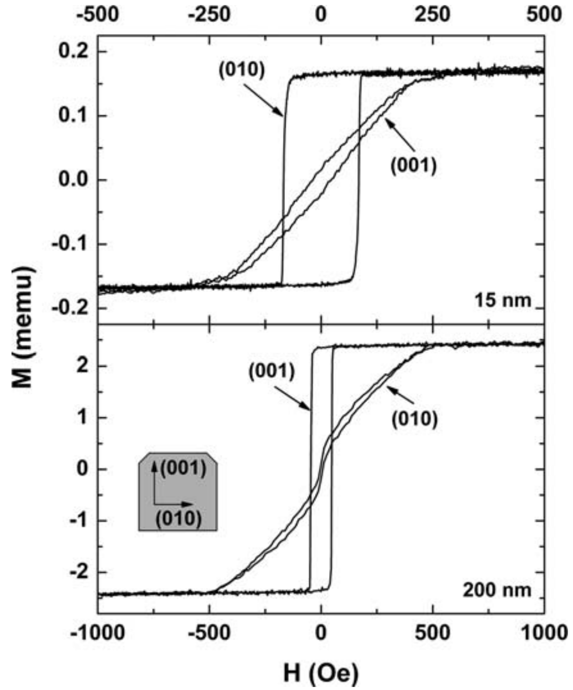

Fig. 17.6 Hysteresis loops for a thin (15 nm) and a thick (200 nm) CrO_2 film along the *c*- and *b*-axis directions

We here attempt to explain the thickness dependence of the magnetic anisotropy and easy axis rotation. We describe the free energy of the system as follows:

$$\begin{aligned} E &= K_0 + K_1 sin^2\theta + K_2 sin^4\theta + (K_{\sigma c} sin^2\theta + K_{\sigma b} cos^2\theta) \\ &= const + K_1 sin^2\theta + K_\sigma sin^2\theta + K_2 sin^4\theta \end{aligned} \tag{17.1}$$

where K_1 and K_2 are the magnetocrystalline anisotropy energy constants; $K_{\sigma b}$ and $K_{\sigma c}$ are the strain anisotropy energy constants associated with the *b*- and *c*-axis directions, respectively.

$$K_\sigma = K_{\sigma c} - K_{\sigma b} = \frac{3}{2}\lambda(\sigma_c - \sigma_b) = \frac{3}{2}\lambda Y(\varepsilon_c - \varepsilon_b)$$

where θ is the angle between the magnetization and the *c*-axis; σ_c and σ_b are the stress components [18]. We have represented K_σ in terms of the strain components in the two directions by using the relationship $K_\sigma = \frac{3}{2}\lambda Y\varepsilon$, where λ is the magnetostriction coefficient, Y is the Young's modulus, and ε is the strain [18].

It is well known that for epitaxial growth on lattice-mismatched substrates the film usually grows coherently strained to match the substrate for thin layers. However, above a critical thickness, dislocations are generated to relieve the misfit strain. By minimizing the sum of the energy of the misfit dislocations and the elastic misfit strain, Matthews and Blakeslee (M–B) [12, 19] have derived the thickness dependence for the residual equilibrium strain,

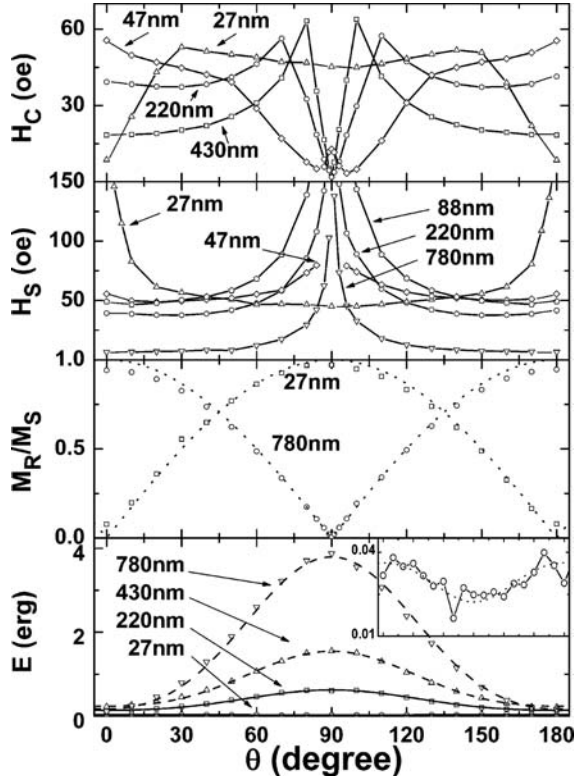

Fig. 17.7 Thickness dependence of the CrO_2 anisotropies. Inset shows the enlarged curve for the 27 nm film

$$\varepsilon = \frac{1 - \nu \cos^2 \varphi}{8\pi(1+\nu)\cos\phi} \frac{b}{t} \ln\left(\frac{4t}{b}\right) \tag{17.2}$$

where b is the magnitude of the Burgers vector of the dislocation, and $\alpha = \dfrac{1 - \nu \cos^2 \varphi}{8\pi(1+\nu)\cos\phi}$ is a constant that depends on the Poisson ratio ($\nu \cong 0.3$), the angles of the Burgers vector with respect to the dislocation line (φ), and the angles between the interface and the normal to the slip plane (ϕ). By neglecting the K_2 term in Eq. (17.1), we can relate the effective magnetic anisotropy energy constant $K_{1eff} = K_1 + K_\sigma$ to the film thickness t,

$$K_{1\text{eff}} = K_1 + \frac{3}{2}\lambda Y \alpha \left[\frac{c}{t}\ln\left(\frac{4t}{c}\right) - \frac{b}{t}\ln\left(\frac{4t}{b}\right)\right] \tag{17.3}$$

In the above equation, we have approximated the magnitudes of the Burgers vectors in the b- and c-directions with the corresponding lattice parameters. From Eq. (17.3), it is seen that the ratio between K_1 and K_σ is proportional to $\dfrac{t}{\ln t + const}$ for films thicker than a few tens of nanometers (i.e., when $t >> b, c$). By analyzing the

anisotropy fields based on the hysteresis loop measured along the hard-axis direction at room temperature (e.g., Fig. 17.6), we have determined the values of K_{1eff} for CrO_2 films over a large range of thicknesses, and a fairly good match has been observed between the model and the experiment [17]. We have carried out X-ray measurements of the off-axis CrO_2 (220) and (202) peaks to determine the in-plane *b* and *c* lattice parameters, and the value of α is determined to be 0.39 from the experimentally measured strain in a 50 nm CrO_2 film. If we assume the Young's modulus to be 2.5×10^{12} dyne/cm^2, as in the case of bulk TiO_2, the magnetostriction coefficient of CrO_2 at room temperature is estimated to be 9.4×10^{-6}. Because of differences in the thermal expansion coefficient between the film and the substrate, the temperature can also induce easy axis reorientation in CrO_2 films, especially for films with thickness around 50 nm.

From the above discussion, it is clear that the nature of the strain relaxation as a function of thickness has a strong influence on the magnetic anisotropy of CrO_2 films. The crystalline and strain anisotropy directions for growth on (100) TiO_2 substrate are orthogonal to each other. If coherent rotation can be achieved for all thicknesses, the easy axis should be along the *c*-direction for films thicker than 50 nm, and along the *b*-direction for films below 50 nm, as suggested by the change in the sign of K_{1eff} [17]. However, our results show that the anisotropy of CrO_2 films is more complicated than a simple switching of easy axis for an intermediate range of thicknesses. In the thickness range of about 50–250 nm, we find that the CrO_2 films do not exhibit a simple uniaxial switching behavior. Figure 17.9(a) shows the hysteresis loops for a 65 nm film with fields applied along various angles relative to the *c*-axis. Clearly, there exist two different switching fields, and they are 90° out of phase, corresponding to the easy axis being along the *b*- or *c*-direction. A similar behavior is observed for thicker films up to about 250 nm, with the *c*-axis switching component increasing in magnitude while the *b*-axis component decaying with increasing film thickness.

The original M–B model was developed for relatively thin films in which the thickness is not much larger than the spacing between neighboring edge dislocation lines, and therefore the strain distribution is assumed to be homogeneous throughout the film. In reality, especially for thick oxide films, the strain is more concentrated near the interface and is gradually relaxed by forming dislocations. This is evidenced from the non-uniform distribution of dislocations at various depths in the films [20, 21]. Using a simple model for the strain distribution throughout the film thickness, we have demonstrated that it is energetically more favorable to form a 90°-domain wall in the middle of the film, and it thus results in the observed double-switching phenomena [17]. The key factors that favor such a phenomena are that the material must have low exchange stiffness constant (A), higher strain anisotropy ($K_b\sim3/2\,\lambda Y\varepsilon$) of the bottom layers, and sufficient thickness to form the domain wall. For films not too thin, and the strain distributed linearly near the substrate–film interface up to thickness t_0, the criterion is $\frac{1}{2}K_b t_0 \geq \frac{\beta}{2}\pi[A(K_b + K_t)]^{1/2}$. Here K_t is the top layer crystalline anisotropy energy constant, β is a dimensionless factor depending on the distribution of strains, and in the above-mentioned case, it is 0.22. CrO_2 satisfies the

criterion because it has a low Curie temperature (low A), a relatively large lattice mismatch with the substrate, and yet can maintain epitaxial growth.

17.3.2 Films Grown on As-Polished TiO_2 Substrates

The growth morphology of the CrO_2 films is critically dependent on the TiO_2 substrate-cleaning procedure utilized prior to deposition. Films grown on as-polished (100)-TiO_2 substrates that are cleaned with organic solvents (acetone and isopropanol) and then rinsed in distilled water are relatively rougher and have a columnar morphology with only a small residual strain [11]. The strain effect is much more pronounced in films grown on substrates that are briefly treated with dilute HF prior to deposition. AFM images confirm that the HF-treated substrates have an atomically smooth surface (Fig. 17.8), and this is the origin of the large strain established in the films described above. Furthermore, the CrO_2 films deposited on top of HF-treated substrates show elongated grains, while those on as-polished substrates show square-shaped grains. This is yet another consequence

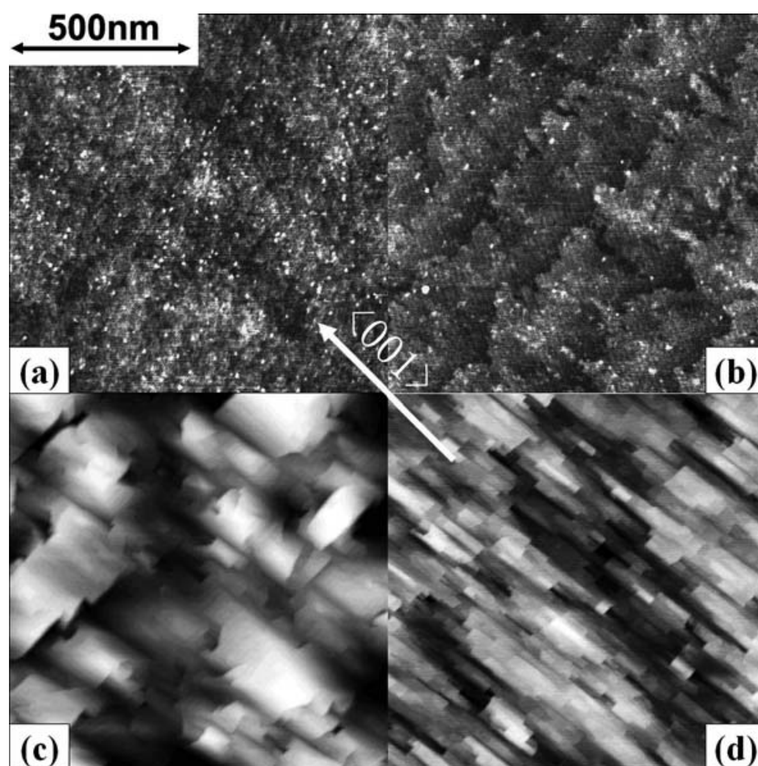

Fig. 17.8 AFM images of (100)-TiO_2 substrates before (**a**) and after (**b**) HF treatment, and CrO_2 films grown on top of them, 65 nm (**c**) and 37 nm (**d**)

of the effect of residual strain. Hereafter, we refer to the CrO_2 films grown on TiO_2 substrates that do not or do undergo the additional HF treatment as strain-free and strained films, respectively. Note that the "strain-free" films are not completely strain free, but exhibit a much lower level of strain as compared to the other type of films. Further improvements in the CrO_2 film morphology is expected with use of TiO_2 substrates that are annealed at high temperatures (700−1,000°C) after the HF chemical treatment [22]. Depending on the miscut angle, the annealing step can lead to formation of large flat terraces with well-defined unit cell steps on the substrate surface.

We next focus on the magnetic properties of the strained and strain-free films. As previously noted, the strained films that grow on atomically ordered substrates are much more heavily strained than the strain-free films.

The effective anisotropy energy constant K_{1eff} can thus be negative, resulting in an easy axis reorientation toward the *b*-axis. In the case of strain-free films, the nucleation and growth of the film occurs more randomly since the surface is rough on an atomic scale. Correspondingly, the strain anisotropy in these films is significantly lower than the crystalline anisotropy. Because of the presence of a large number of defects, the RMS roughness of these films is typically about twice as large as those of the strained films. Despite an inferior crystalline quality, these films exhibit magnetic switching behavior close to that observed in bulk single crystals of CrO_2. Figure 17.9 shows the hysteresis loops of a strained and a strain-free

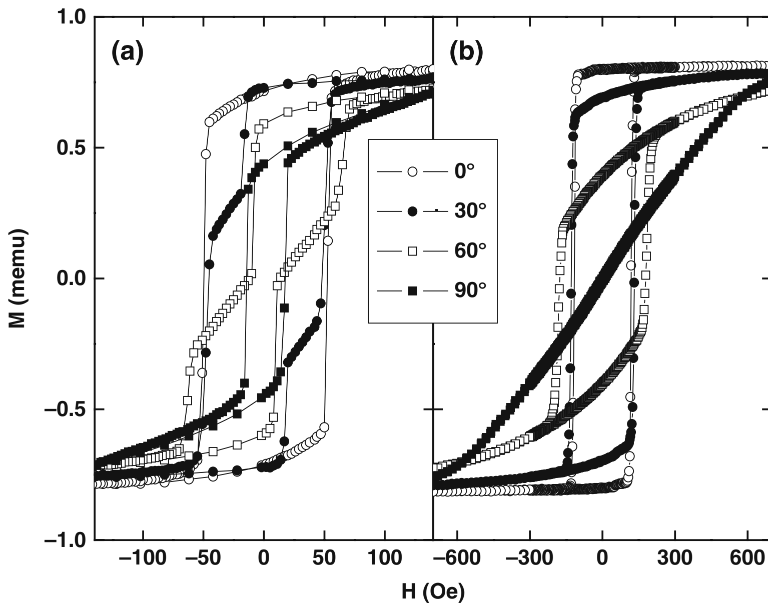

Fig. 17.9 Comparison of the hysteresis loops for a heavily strained (**a**) and a relatively strain-free (**b**) CrO_2 film. Both films are 65 nm. The indicated angles are the field direction with respect to the film *c*-axis

film, both of which are nominally 65 nm thick. The double-switching phenomena, resulting from non-uniform distribution of strain, that normally appear in the heavily strained films of intermediate thickness, are not observed in the strain-free films. Furthermore, because of the lack of any significant influence of strain in the latter, the magnetic anisotropy is close to being uniaxial with a much more uniform magnetization, resulting in a higher nucleation field.

The CrO_2 films grown on TiO_2 substrates can be readily etched by chemical treatment using a commercial chromium etchant solution. The cleaned substrates can then be reused (after HF pre-treatment) for growth of CrO_2 films. We have found that TiO_2 substrates that have been repeatedly re-cleaned also lead to the growth of strained CrO_2 films, but progressively less so with increasing usage as compared to virgin HF-treated substrates [11]. This is not surprising considering that the surface becomes increasingly rougher with each deposition and surface cleaning cycle. In addition, we have found that ion milled substrates also lead to the growth of less-strained films. This suggests that it is important to start with an atomically smooth surface in order to obtain coherently strained epitaxial films.

17.4 CrO_2-Based Heterostructures

We have taken advantage of the fact that the switching field of CrO_2 thin films is strain dependent to achieve differential magnetic switching in CrO_2/epitaxial spacer layer/CrO_2 heteroepitaxial structures without resort to exchange biasing of one of the magnetic layers. Exchange biasing would in general require an additional antiferromagnetic layer that can potentially degrade the epitaxy. The spacer layers we have explored include SnO_2, RuO_2, and Cr_2O_3. In all cases, the bottom CrO_2 layer is grown on an atomically smooth TiO_2 surface as described above, while the top layer is deposited on top of a somewhat rougher spacer layer that is either formed naturally (Cr_2O_3) or deposited by CVD (SnO_2, RuO_2), and is less strained than the bottom layer. With spacer layer thicknesses of ≥ 2 nm, the top and bottom CrO_2 layers can be magnetically decoupled (Fig. 17.10). Indeed, the XRD results in Fig. 17.11 show that the two layers are strained differently, as reflected by the presence of two separate peaks in the $\theta - 2\theta$ scans. However, when using Cr_2O_3 as a spacer layer, the two peaks are indistinguishable, suggesting that the very thin Cr_2O_3 reverts back to CrO_2 during the deposition step for the top CrO_2 layer. The extremely low resistance of MTJs fabricated using $CrO_2 - CrO_2$ layers separated by a natural barrier provides further evidence of the absence of interface Cr_2O_3 after the second deposition step. Interestingly, high-resolution TEM images show that the formation of either RuO_2 or SnO_2 on top of the CrO_2 surface also results in the removal of the native Cr_2O_3 surface layer [15, 23], but at the expense of increased interface roughness. The increased interface roughness, or what we term intermixing, has a significant influence on the spin polarized transport as described later. We have observed substantial magnetoresistance (MR) in these heterostructures with using Co as a counter-electrode. But the observed MR values are far lower than what would be expected based on the simple Julliere model. Surprisingly, negligible MR has been

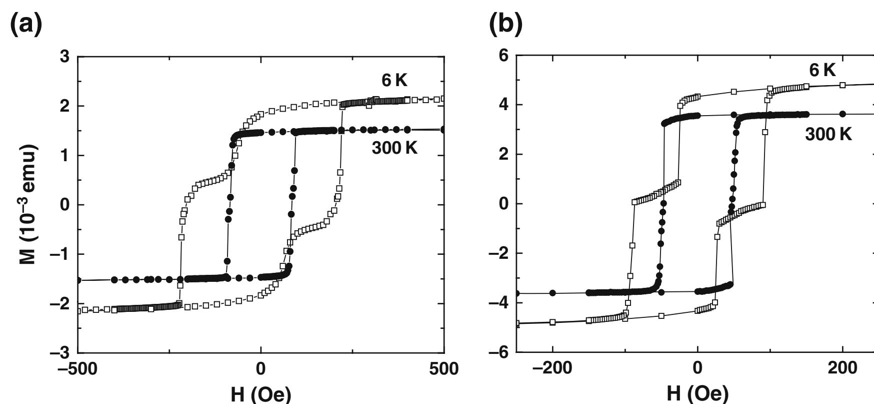

Fig. 17.10 Hysteresis loops for (**a**) 80 nm CrO_2/3 nm SnO_2/60 nm CrO_2 trilayer; (**b**) 160 nm CrO_2/3 nm RuO_2/140 nm CrO_2 trilayer measured at 6 and 300 K

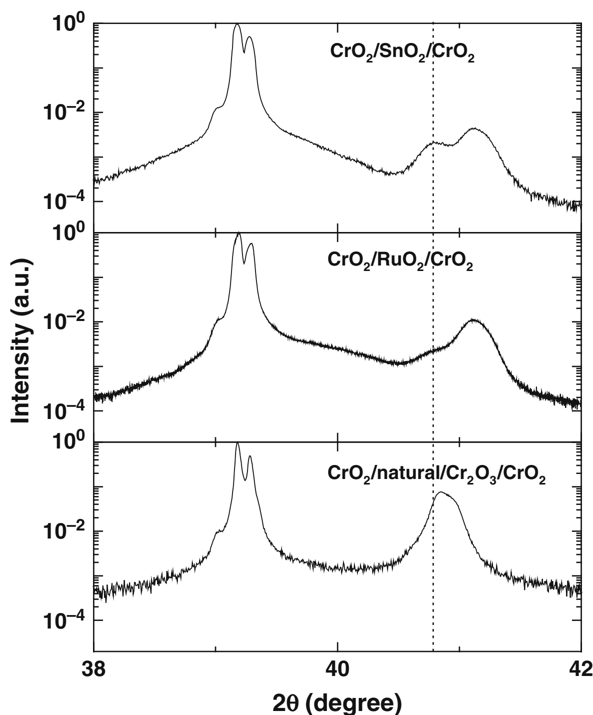

Fig. 17.11 XRD of epitaxial trilayers with thin SnO_2, RuO_2, and Cr_2O_3 spacer layers sandwiched between two magnetic CrO_2 layers. All the barrier layers are in the thickness range of 2−3 nm. *Dashed line* indicates the bulk CrO_2 (200) peak position

observed in the more interesting fully epitaxial CrO_2 heterostructures using SnO_2 and RuO_2 spacer layers.

17.4.1 Epitaxial SnO_2 Barrier Layer

Despite a large difference in the lattice parameters, epitaxial SnO_2 ($a = b =$ 0.4737 nm, $c = 0.3185$ nm; lattice mismatch with CrO_2 being 7.2 and 9.2%, respectively) layers can be deposited on top of CrO_2 in a separate CVD step. The epitaxy has been confirmed using both TEM and off-axis XRD measurements [23]. We have used tin (IV) iodide as a precursor for the growth of thin SnO_2 layers. Figure 17.12 shows a cross-sectional *Z*-contrast image of the interface region for a 50 nm CrO_2/20 nm SnO_2 heterostructure. The two layers are well aligned and form an abrupt interface, with no evidence of an interfacial layer of Cr_2O_3, overall indicating that the SnO_2 layer is indeed highly crystalline and uniform.

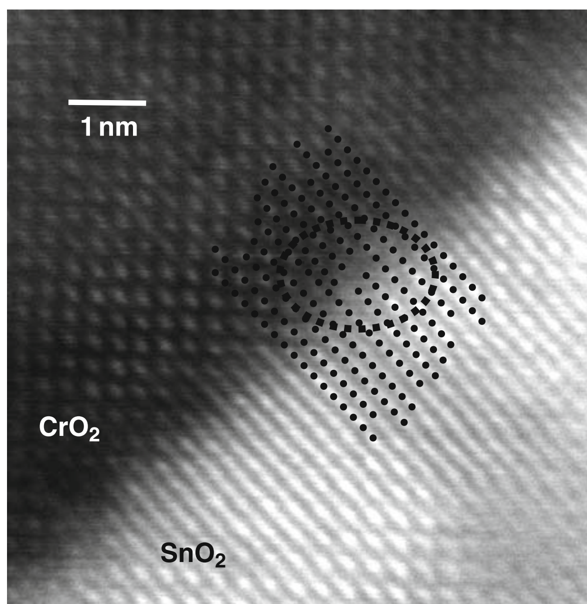

Fig. 17.12 High-resolution STEM image at the CrO_2/SnO_2 interface of a film deposited on a (100) TiO_2 substrate. One of the edge dislocation cores resulting from the lattice mismatch is highlighted. (Courtesy of M. Varela and S. J. Pennycook, Oak Ridge National Laboratory)

Amongst the three layers investigated, SnO_2 is the barrier material that has yielded the highest MR in the CrO_2-based systems. Using Co as counter-electrode, the MR is about 14% at 10 K for an optimized barrier layer thickness of about 1.7 nm. Figure 17.13b shows one example of such a MTJ. Since SnO_2 is a semiconductor, MTJs based on it exhibit some unusual behavior. Firstly, the

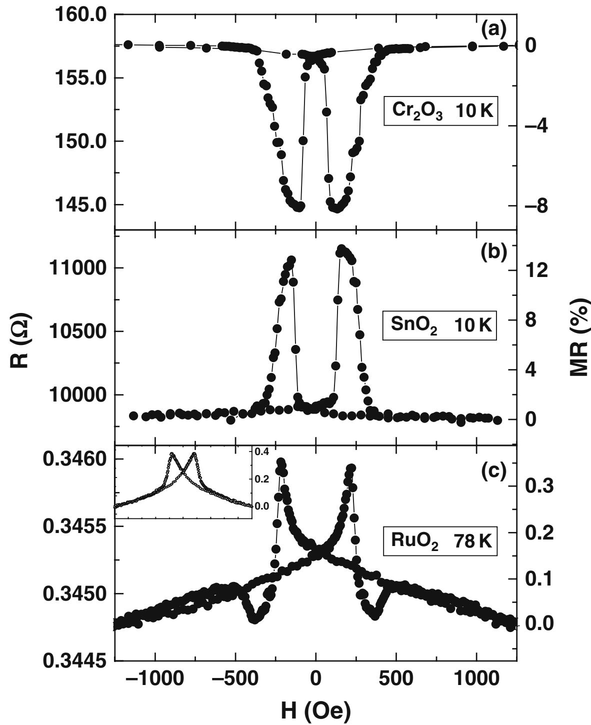

Fig. 17.13 Comparison of the MR loops in CrO_2−Co-based junctions with natural Cr_2O_3, epitaxial SnO_2 and RuO_2 as spacer layers, respectively. Junction areas are $35 \times 7\ \mu m^2$. Inset in (**c**) shows the AMR signal measured from the CrO_2 bottom electrode

tunneling magnetoresistance (TMR) is negative for very small SnO_2 thicknesses, reverses sign at around 0.8 nm, and then peaks for a barrier thickness of 1.7 nm. This behavior is shown in Fig. 17.14. As the SnO_2 thickness is reduced, the chemical bonding at the top interface shifts from being predominantly Co−SnO_2 to being mostly Co−Cr_2O_3. For small SnO_2 thicknesses, the tunneling is dominated by the negatively polarized d-like electrons due to $sd\sigma$ bonding, whereas for larger thicknesses positively polarized s-like electrons dominate because of $ss\sigma$ bonding. The increase of the TMR is correlated with the exponential increase of the junction RA product, consistent with an elastic tunneling process. As the barrier thickness is increased further, a cross-over into the diffusive regime is evidenced.

In this case, the hopping mechanism dominates, and the TMR decreases with increasing SnO_2 thickness. Interestingly, the RA value also decreases as the barrier thickness increases. A rapid drop in the SnO_2 resistivity with film thickness has been reported for as-grown epitaxial SnO_2 films using CVD [24]. This is dependent on the deposition method used for the growth of SnO_2. In an oxygen environment at elevated temperatures, thinner CVD-grown SnO_2 films are closer to being stoichiometric, while thicker films tend to develop more oxygen vacancies.

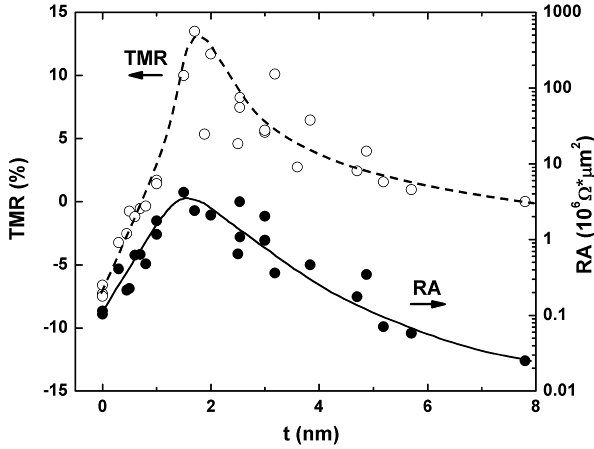

Fig. 17.14 Thickness dependence of TMR and junction RA at 10 K and 1 mV bias voltage; the *dashed and solid lines* are for visual guidance

From the results, we can estimate the concentration of oxygen vacancies in the barrier layer. For this, we assume the existence of two parallel conduction channels – a ballistic tunneling channel and a diffusive channel. When the direct conductance becomes equal to the tunneling conductance, a cross-over in the RA value is observed. Assuming that at the cross-over point the conductances of the two channels are equal, we can estimate the barrier resistivity at 10 K to be about 6×10^5 Ω-cm. For the 8 nm barrier, which is sufficiently thick that direct conduction dominates, the barrier resistivity is estimated to be only 3×10^2 Ω-cm. The large decrease of the SnO_2 resistivity is a signature of the dramatic increase in the concentration of oxygen vacancies in the thicker SnO_2 films, as well as the associated decrease in the carrier mobility [25]. Even so, using an approximate mobility value of 7 $cm^2/V.s$ [26], we estimate a carrier concentration of only 3×10^{15} cm^{-3} for the 8 nm barrier at 10 K, and the estimated oxygen vacancy (assuming each O vacancy contributes two charge carriers) is below 0.03 ppm. If the spin coherence can be maintained in the direct conduction pathway, the MR should not change significantly with the emergence of this conduction channel. However, because of large spin–orbit coupling, the Sn atoms ($Z = 50$) are strong spin scattering centers, and the spin diffusion length in SnO_2 is only about 4 nm as estimated from the decay rate of the MR.

Figure 17.15 shows the bias-dependence results for one of the SnO_2-based MTJ. A clear signature of defect mediated tunneling is inferred from the data. Firstly, the samples exhibit a rapid drop in TMR with applied bias voltage, which points to the existence of spin-flip scattering resulting from impurities in the barrier [27]. Two sources of impurities are possible – Cr ions and oxygen vacancies. The former is a consequence of the intermixing at the SnO_2/CrO_2 interfaces, and the latter has been theoretically predicted and experimentally observed in SnO_2, resulting in its semiconducting properties [28]. Secondly, a clear TMR reversal with applied bias voltage is observed [29,30,31]. Unlike previous findings [32,33,34], the TMR

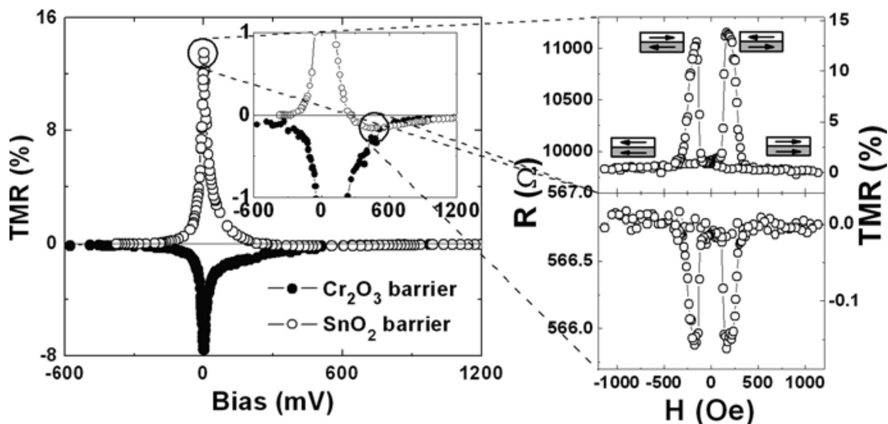

Fig. 17.15 Comparison of bias dependence for CrO_2/Co junctions with 2 nm SnO_2 barriers (*white*) and natural Cr_2O_3 barriers (*black*), inset shows the zoomed-in region. The magnetoresistance of the SnO_2 sample at 1 and 450 mV bias values are shown on the *right*. T = 10 K

reversal with bias cannot be attributed to the DOS peak in the Co 3*d* minority bands at about 400 mV bias [33, 34], since that would imply a negative TMR at zero bias and a positive TMR at high-bias values. Based on the model proposed by Tsymbal et al. [29,30,31], we attribute the observed TMR reversal at higher bias voltages (250−400 mV depending on the barrier thickness, Fig. 17.15) to the existence of impurity levels within the barrier.

Figure 17.16 illustrates the tunneling spectra for an MTJ with a 2.5 nm SnO_2 barrier sandwiched between two epitaxial CrO_2 layers. The nonlinear $I-V$ characteristics provide evidence of tunneling transport. However, the large temperature dependence of the conductance indicates that the tunneling is dominated by multistep hopping instead of direct tunneling. Surprisingly, no MR has been observed in these MTJs. On the other hand, a sample prepared in the same run, but with Co as the top electrode, showed finite TMR at 10 K (Fig. 17.13b). The results are puzzling, and we believe part of the problem is in the rough/intermixed interfaces in the all-heteroepitaxial structures. The deposition of the second CrO_2 layer is performed at an elevated temperature, which may introduce additional spin scattering centers at the interfaces and also inside the barrier layer itself. High-resolution microscopy images of the top interface in these epitaxial heterostructures are needed in order to identify the influence of deposition of the top layer.

17.4.2 Epitaxial RuO_2 Barrier Layer

Epitaxial RuO_2 thin films can also be deposited on TiO_2 and CrO_2 using CVD methods [15, 35]. The lattice parameters of RuO_2 ($a = b = 0.4499$ nm and $c = 0.3107$ nm) provide a better lattice match with CrO_2 in the two in-plane directions (1.8 and 5.0%, respectively) than with SnO_2. For the growth of RuO_2, we have

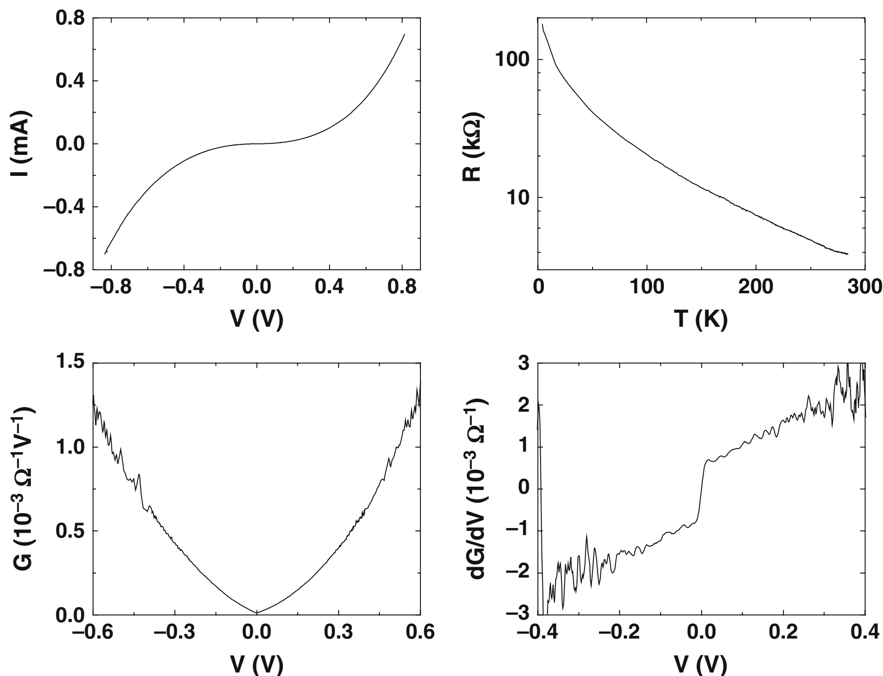

Fig. 17.16 Tunneling spectroscopy measurements for a 100 nm CrO_2/2.5 nm SnO_2/200 nm CrO_2 MTJ. The junction area is 35×7 μm^2, and the measurement temperature $T = 10$ K

used tris(2,2,6,6-tetramethyl-3,5-heptanedionato) ruthenium(III) ($Ru(TMHD)_3$) as a precursor. RuO_2 exhibits good metallic behavior, with room temperature resistivity of ~40 μΩ-cm, and can thus be used as a spacer layer in GMR structures. $CrO_2 - RuO_2 - CrO_2$ should be an "ideal" spintronic system based on electronic structure. For parallel alignment of the magnetizations of the two CrO_2 layers, the resistance should be extremely small because of the close majority band matching between CrO_2 and RuO_2. For anti-parallel alignment, however, the resistance should be extremely high, giving ~100% magnetoresistance for the ideal case.

The detailed structural and electrical properties of CVD-deposited RuO_2 thin films are provided in [15]. Using CrO_3 as a precursor for the CrO_2 growth, and $Ru(TMHD)_3$ for depositing RuO_2, we have the advantage that the entire structure can be grown under process conditions compatible with the growth and stability of CrO_2. However, although both films can be grown under similar conditions, it is still necessary to stop the growth after each layer and exchange the precursors to grow the next layer. This is because both of the precursors are solids at room temperature, and there is no convenient scheme for switching from one to the other in situ using our setup.

As the TEM micrograph in Fig. 17.17 shows, the RuO_2 spacer forms a continuous spacer layer in the heterostructure, but the RuO_2/CrO_2 interfaces are quite rough and intermixed. Surprisingly, we find that that despite stopping the growth

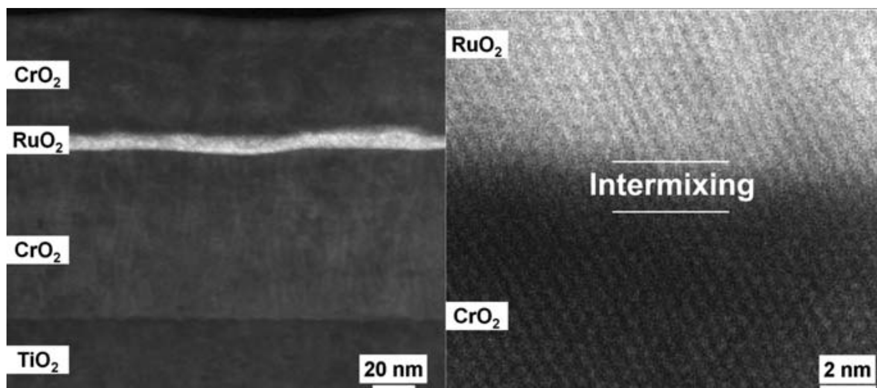

Fig. 17.17 HRTEM of a $CrO_2/RuO_2/CrO_2$ heteroepitaxial structure. The *right side figure* shows a high-magnification image of the interface intermixed region (adapted from Ref. [35])

and exchanging precursors after the CrO_2 deposition, the typical Cr_2O_3 natural barrier on the CrO_2 surfaces is absent after the RuO_2 deposition (similar to that of $CrO_2 - SnO_2$ discussed previously). This yields a highly conductive interface that has a resistance at least four orders of magnitude lower than if the Cr_2O_3 were present. The high-resolution TEM (shown as an inset in Fig. 17.17) and electron diffraction pattern at and around the CrO_2/RuO_2 interface reveals a highly intermixed region $\sim$2 nm wide, with a lattice parameter between those of CrO_2 and RuO_2. In our interpretation, this intermixed region results from the transformation of a Cr_2O_3 surface layer formed after CrO_2 deposition (but before RuO_2 deposition) into the rutile structure upon RuO_2 deposition, giving a CrO_2/RuO_2 mixture.

So far, we have observed very limited MR in these heteroepitaxial structures (Fig. 17.13c). At least part of the reason for the low MR might be from poor magnetic ordering and spin alignment at the mixed CrO_2/RuO_2 (001) interface. Preliminary first principles calculations suggest that non-collinear spins resulting from interface mixing may play a role. In these calculations, we find that the moments of the Cr atoms prefer to align at an angle of $\sim 150^\circ$, while the Ru atoms develop a small moment that aligns opposite to that of the sum of two Cr atoms [36]. Such non-collinear spin arrangements, which will depend on the details of the Cr and Ru occupation of the disordered rutile structure, are expected to cause mixing of the spin channels, drastically reducing the GMR effect.

17.4.3 VO_2 Barrier Layer

VO_2 is yet another rutile oxide that has been investigated extensively, primarily for its unique metal–insulator transition occurring at around 340 K resulting in dramatic change in electrical resistivity. Because of the large change in the resistance of the spacer layer at the transition temperature, a change in the magneto-transport

characteristics from TMR to CPP-GMR would be expected in $CrO_2 - VO_2 - CrO_2$ heterostructures. This may involve both changes in the MR magnitude as well as its bias dependence, and could lead to novel effects to be exploited for new applications for storage and memory devices.

Chemical vapor deposition can be used to grow VO_2 thin films at relatively low temperatures [37]. We have used vanadium (III) acetylacetonate as a precursor for the growth of VO_2 films. Above the transition temperature, VO_2 has a rutile structure ($a = b = 0.4556$ nm, $c = 0.2859$ nm), which matches fairly well with CrO_2 (3.1 and −2.0%). Below the transition temperature, VO_2 has a monoclinic structure ($a = 0.5743$, $b = 0.4517$, $c = 0.5375$, and $\beta = 122.6°$). Figure 17.18 shows the M−I transition in an as-deposited epitaxial VO_2 film (∼100 nm thick) on (100) TiO_2 substrate. The high quality of the film is confirmed by the sharpness of the transition and the associated hysteretic behavior. Vanadium has a number of stable oxidization states, and different phase(s) of vanadium oxide (VO, V_2O_3, VO_2, V_2O_5 can be stabilized in thin film form, particularly when they are very thin. XPS result shows that a 2−3 nm thick VO_x film deposited on top of a CrO_2 film is primarily V_2O_5 (Fig. 17.19), instead of the desired VO_2 phase. Indeed, preliminary measurements on MTJs fabricated using such a VO_x barrier with Co counter-electrode did not show any evidence of an M−I transition above room temperature. The TMR in these junctions is negative, similar to that observed with a natural Cr_2O_3 barrier.

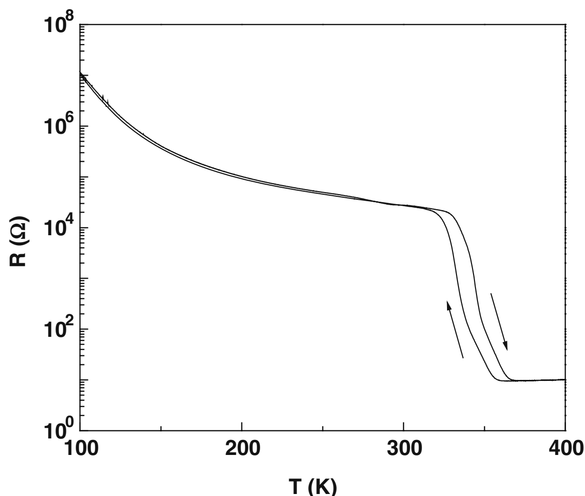

Fig. 17.18 Metal–insulator transition in an epitaxial VO_2 film (∼100 nm)

17.4.4 TiO_2 Barrier Layer

TiO_2 is the most common rutile structure oxide. The name rutile comes from the mineral composed mainly of TiO_2. The lattice parameter of rutile TiO_2 are $a = b = 0.4594$ nm, $c = 0.2958$ nm, providing a good match with CrO_2 (3.9 and 1.4%).

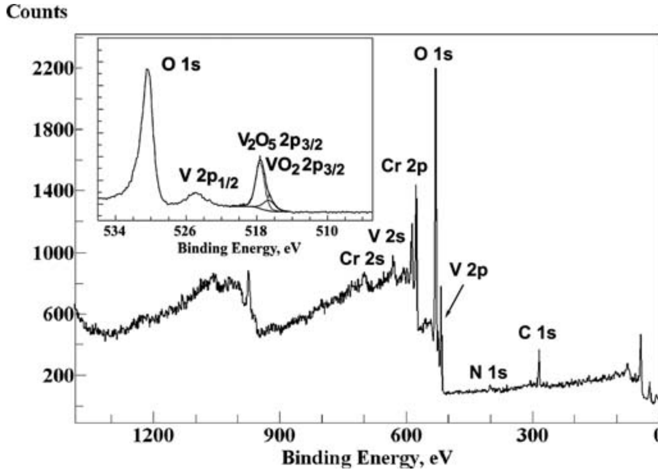

Fig. 17.19 XPS result for a thin VO_x film deposited on top of a CrO_2 film. Inset shows the O 1s and V 2p spectra. Peakfit of the V 2p3/2 line suggest the presence of VO_2 (23%) and V_2O_5 (77%) states

Indeed, as a substrate material, rutile TiO_2 provides an excellent template for the epitaxial growth of CrO_2 films as discussed earlier. We have used titanium(IV) isopropoxide as a precursor for the growth of TiO_2 films. Although rutile TiO_2 is the most stable and abundant phase of TiO_2, the primary challenge is to stabilize TiO_2 in its rutile structure at low enough temperatures on top of CrO_2 since the latter readily decomposes at temperatures much higher than 400°C (see next section). At lower temperatures, the anatase and brookite phases of TiO_2 are formed, and they can be converted to the rutile phase only at temperatures above 750°C. Direct deposition of rutile TiO_2 films using CVD at temperatures as low as 490°C has been reported [38]. With plasma enhancement, it is possible to reduce the temperatures even lower [39]. However, using standard CVD, we have thus far succeeded in only growing the anatase phase of TiO_2 at temperatures compatible with the stability of CrO_2. To the best of our knowledge, there have been no other reports in the literature on the growth and transport measurements of heteroepitaxial CrO_2/TiO_2-based MTJs.

17.4.5 Cr_2O_3 Barrier Layer

Cr_2O_3, an antiferromagnetic insulator ($T_N = 307$ K), is the most stable phase in the Cr oxide family. The formation of the different phases of Cr oxide by CVD is dependent on the deposition temperature, background pressure, and lattice mismatch with the substrate [40]. The air-exposed surface of an as-grown CrO_2 film tends to be reduced to Cr_2O_3 forming a native insulating layer. This insulating layer can be utilized as a tunneling barrier. From the STEM and EELS data shown in Fig. 17.20, the thickness of the barrier is estimated to be ~2 nm. An example of the TMR measured in a CrO_2/natural barrier/Co tunnel junction is shown in Fig. 17.12a, and the first results on such junctions were reported in [41]. One striking feature of the natural

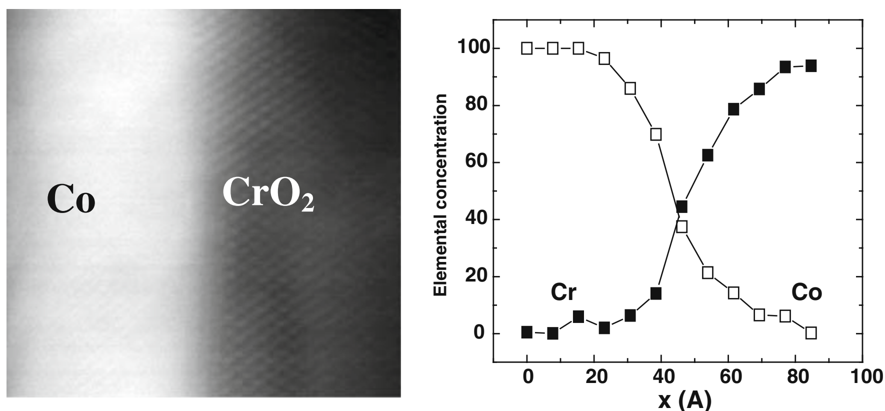

Fig. 17.20 STEM image and EELS line scan data for a Co/natural barrier/CrO_2 stack. The interface chemical width, which includes the natural barrier, is about 2 nm. (Courtesy of M. Varela and S. J. Pennycook, Oak Ridge National Laboratory)

barrier-based MTJs is the inverse sign of the TMR, which has been attributed to the dominance of *d*-like tunneling electrons [23]. The thickness of the Cr_2O_3 can be controllably increased by thermally annealing the CrO_2 films. The transverse susceptibility results on CrO_2 films that have been partially converted to Cr_2O_3, by annealing in an oxygen environment at 450°C for different lengths of time, have been reported in [42]. Figure 17.21a shows the XRD pattern for a 200 nm CrO_2 film after thermal annealing. Clearly the CrO_2 peak intensity decreases with increasing anneal time, with the emergence of the Cr_2O_3 (110) and (006) product peaks. The corresponding magnetic hysteresis loops of the samples are shown in Fig. 17.21b, confirming the decrease in magnetization with increasing anneal time.

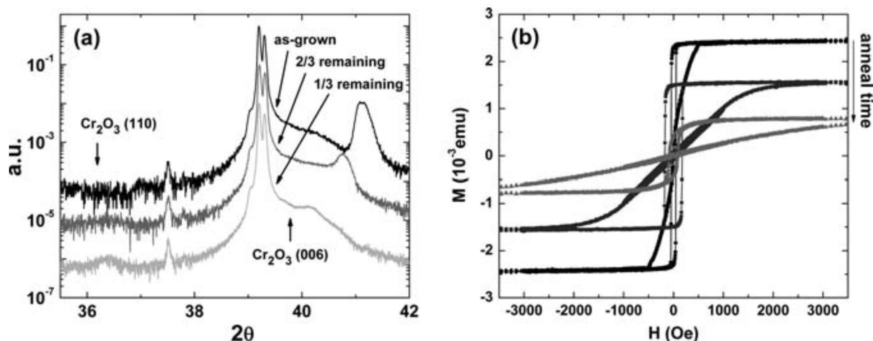

Fig. 17.21 (**a**) XRD for CrO_2 films partially decomposed into Cr_2O_3. The starting CrO_2 film thickness is around 200 nm, and the curves are systematically shifted upwards by a decade for clarity. (**b**) Hysteresis loops for the samples with increasing anneal time

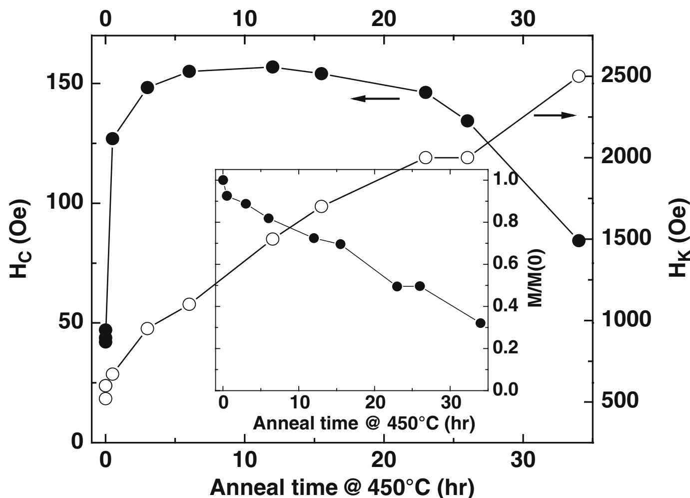

Fig. 17.22 Variations in the coercive and anisotropy fields for thermally decomposed $CrO_2-Cr_2O_3$ bilayer structures. Inset shows the decrease of the saturation moment with increasing anneal

Large changes in the coercive and anisotropy fields are observed in these $CrO_2-Cr_2O_3$ bilayer structures. The anisotropy field, H_K, increases monotonically with increasing thickness of Cr_2O_3, while the coercivity, H_C, exhibits an initial sharp increase and then decreases slowly with further annealing (Fig. 17.22). The dramatic changes in the film magnetic properties indicate the presence of exchange interactions between the AFM Cr_2O_3 and FM CrO_2. However, the exchange bias in such an FM-AFM system is quite small. From the exchange bias measured for a 100 nm CrO_2 film that is 3/4th decomposed into Cr_2O_3, the exchange energy is estimated to be only $\sim$0.028 erg/cm^2 at 6 K, and the exchange field further drops to about 1/3rd its initial value after cycling through saturation ten times (the training effect). From the decrease in the magnetic moment with anneal time (Fig. 17.22 inset), the formation rate of Cr_2O_3 from CrO_2 decomposition is estimated to be about 4 nm/h. The TMR measured in junctions with thicker Cr_2O_3 barriers formed by annealing still remains negative, and the junction resistance increases slowly. For example, for a Cr_2O_3 layer thickness of 10 nm, the junction resistance is measured to be only 10 times higher than that for a natural barrier of 2 nm thickness. Furthermore, the junction resistance is strongly temperature dependent. These results suggest that the Cr_2O_3layer has a high concentration of defects, and the conduction through such a barrier most likely involves multistep hopping instead of direct tunneling.

Acknowledgments Most of the work reviewed in this chapter has been carried out by the authors over a period of several years in collaboration with a number of other colleagues. We express our gratitude to all the collaborators for their contributions, support, and help. In particular, we would like to acknowledge Alexander Anguelouch, William Butler, Chia-Ling Chien, Supratik Guha, Srikanth Hariharan, Patrick LeClair, Xin-Wei Li, Stephen Pennycook, Maria Varela, and Gang Xiao.

References

1. K. Schwarz, *J. Phys. F: Met. Phys.* **16**, L211 (1986).
2. S. P. Lewis, P. B. Allen, and T. Sasaki, *Phys. Rev. B* **55**, 10 253 (1996).
3. M. A. Korotin, V. I. Anisimov, D. I. Khomskii, and G. A. Sawatzky, *Phys. Rev. Lett.* **80**, 4305 (1998).
4. R. J. Soulen, J. M. Byers, M. S. Osofsky, B. Nadgorny, T. Ambrose, S. F. Cheng, P. R. Broussard, C. T. Tanaka, J. Nowak, J. S. Moodera, A. Barry, and J. M. D. Coey, *Science* **282**, 85 (1998).
5. Y. Ji, G. J. Strijkers, F. Y. Yang, C. L. Chien, J. M. Byers, A. Anguelouch, G. Xiao, and A. Gupta, *Phys. Rev. Lett.* **86**, 5585 (2001).
6. A. Anguelouch, A. Gupta, G. Xiao, D. W. Abraham, Y. Ji, S. Ingvarsson, and C. L. Chien, *Phys. Rev. B* **64**, 180408R (2001).
7. S. Ishibashi, T. Namikawa, and M. Satou, *Mater. Res. Bull.* **14**, 51 (1979).
8. X. W. Li, A. Gupta, and G. Xiao, *Appl. Phys. Lett.* **75**, 713 (1999).
9. K. Suzuki and P. M. Tedrow, *Solid State Comm.* **107**, 583 (1998).
10. A. Gupta, X. W. Li, S. Guha, and G. Xiao, *Appl. Phys. Lett.* **75**, 2996 (1999).
11. G. X. Miao, G. Xiao, and A. Gupta, *Phys. Stat. Sol. A* **203**, 1513 (2006).
12. J. W. Matthews and A. E. Blakeslee, *J. Cryst. Growth* **27**, 118 (1974).
13. T. Suzuki, Y. Nishi, and M. Fujimoto, *Philos. Mag. A* **79**, 2461(1999).
14. S. H. Oh, C. G. Park, *J. Appl. Phys.* **95**, 4691 (2004).
15. G. X. Miao, A. Gupta, G. Xiao, and A. Anguelouch, *Thin Solid Films* **478**, 159 (2004).
16. D. S. Rodbell, *J. Phys. Soc. Jpn.* **21**, 1224 (1966).
17. G. X. Miao, G. Xiao, and A. Gupta, *Phys. Rev. B* **71**, 094418 (2005).
18. B. D. Cullity, *Introduction to Magnetic Materials* (Addison-Wesley, London, 1972).
19. J. W. Matthews, *J. Vac. Sci. Technol.* **12**, 126 (1975).
20. S. H. Oh and C. G. Park, *J. Appl. Phys.* **95**, 4691 (2004).
21. Y. Konishi, M. Kasai, M. Izuma, M. Kawasaki, and Y. Tokura, *Mater. Sci. Eng. B* **56**, 158 (1998).
22. Y. Yamamoto, K. Nakajima, T. Ohsawa, Y. Matsumoto, and H. Koinuma, *Jpn. J. Appl. Phys.* **44**, L511 (2005).
23. G. X. Miao, P. LeClair, A. Gupta, G. Xiao, M. Varela, and S. Pennycook, *Appl. Phys. Lett.* **89**, 022511 (2007).
24. A. Rosental, A. Tarre, A. Gerst, J. Sundqvist, A. Harsta, A. Aidla, J. Aarik, V. Sammelselg, and T. Uustare, *Sens. Actu. B* **93**, 552 (2003).
25. C. G. Fonstad and R. H. Rediker, *J. Appl. Phys.* **42**, 2911 (1971).
26. J. E. Dominguez, L. Fu, and X. Q. Pan, *Appl. Phys. Lett.* **81**, 5168 (2002).
27. J. S. Moodera, J. Nassar, and G. Mathon, *Annu. Rev. Mater. Sci.* **29**, 381 (1999).
28. A. Kilic, A. Zunger, *Phys. Rev. Lett.* **88**, 095501-1 (2002), and references therein.
29. E. Y. Tsymbal, D. G. Pettifor, *Phys. Rev. B* **64**, 212401-1 (2001).
30. E. Y. Tsymbal, A. Sokolov, I. F. Sabirianov, and B. Doudin, *Phys. Rev. Lett.* **90**, 186602-1 (2003).
31. L. Sheng, D. Y. Xing, and D. N. Sheng, *Phys. Rev. B* **69**, 132414 (2004).
32. M. Sharma, S. X. Wang, and J. H. Nickel, *Phys. Rev. Lett.* **82**, 616 (1999).
33. J. M. Teresa, A. Barthelemy, A. Fert, J. P. Contour, R. Lyonnet, F. Montaigne, P. Seneor, and A. Vaures, *Phys. Rev. Lett.* **82**, 4288 (1999).
34. J. M. Teresa, A. Barthelemy, A. Fert, J. P. Contour, F. Montaigne, and P. Seneor, *Science* **286**, 507 (1999).
35. G. X. Miao, A. Gupta, H. Sims, W. H. Butler, S. Ghosh, and G. Xiao, *J. Appl. Phys.* **97**, 10C924 (2005).
36. G. X. Miao, Ph. D. thesis (Brown University, Providence, RI, 2006).
37. M. B. Sahana, G. N. Subbanna, and S. A. Shivashankar, *J. Appl. Phys.* **92**, 6495 (2002).
38. M. Schuisky and A. Harsta, *J. Phys. IV* **9**, 381 (1999).

39. Y. Kumashiro, A. Kinoshita, Y. Takaoka, and S. Murasawa, *J. Ceramic Soc. Jpn.* **101**, 514 (1993).
40. P. G. Ivanov, S. M. Watts, and D. M. Lind, *J. Appl. Phys*. **89**, 1035 (2001).
41. A. Gupta, X. W. Li, and G. Xiao, *Appl. Phys. Lett.* **78**, 1894 (2001).
42. N. A. Frey, S. Srinath, H. Srikanth, M. Varela, S. Pennycook, G. X. Miao, and A. Gupta, *Phys. Rev. B* **74**, 024420 (2006).